Observational constraints on fractional holographic dark energy in the light of DESI DR2*

Qihong Huang (黄启洪)[1†] Yuchen Zhang (张宇辰)[2] Bing Xu (徐兵)[3] Kaituo Zhang (张开拓)[4]

[1]School of Physics and Electronic Science, Zunyi Normal University, Zunyi 563006, China
[2]Department of Physics, Key Laboratory of Low Dimensional Quantum Structures and Quantum Control of Ministry of Education, and Hunan Research Center of the Basic Discipline for Quantum Effects and Quantum Technologies, Hunan Normal University, Changsha 410081, China
[3]School of Electrical and Electronic Engineering, Anhui Science and Technology University, Bengbu 233030, China
[4]Department of Physics, Anhui Normal University, Wuhu 241000, China

Abstract: Based on the fractional entropy from fractional quantum mechanics, fractional holographic dark energy (FHDE) has been proposed with the Hubble horizon as the IR cutoff (FHDEH). We extend this framework by adopting the future event horizon and the particle horizon as the IR cutoff and proposing the FHDEF and FHDEP models. Using the SN+OHD+DESI DR2 dataset to constrain these models, we find that all three models provide a marginally lower $\chi^2_{\rm min}$ compared to ΛCDM but without significant preference according to AIC and BIC. When CMB distance priors are included, the FHDEH and FHDEP models are strongly ruled out. We further analyze the cosmological evolution for these models, and find that only the FHDEF model predicts nearly identical evolutions of Ω_m and $\Omega_{\rm de}$ to those of the ΛCDM model across cosmic history, but its deceleration parameter q deviates from the ΛCDM model in the future, indicating richer late time dynamics beyond the standard ΛCDM cosmology.

Keywords: holographic dark energy, observational constraints, DESI DR2

DOI: 10.1088/1674-1137/ae9926 **CSTR:** 32044.14.ChinesePhysicsC.50115104

I. INTRODUCTION

Many cosmological observations suggest that the universe is experiencing an accelerated expansion [1–6]. A natural way to explain this remarkable phenomenon is to introduce dark energy [7], with the cosmological constant representing the simplest theoretical candidate and providing an excellent fit to a wide range of observational data [8]. However, the cosmological constant model faces some problems [9, 10]. To alleviate these problems, holographic dark energy (HDE) has been proposed and has attracted lots of attention [11–15], and its cosmological implications have been investigated from both observational constraints [16–19] and dynamical evolution [20, 21]. Its framework is based on the holographic principle, motivated by black hole thermodynamics, and on the connection between the ultraviolet cutoff of a quantum field theory and the largest distance scale of the theory. Within the HDE framework, the choice of horizon entropy is crucial, since it uniquely determines the energy density, giving rise to various HDE models [15]. For instance, the original HDE model arises from taking the Bekenstein– Hawking entropy as the horizon entropy [11–13], while Tsallis HDE models are based on Tsallis entropy as a generalization of the standard Boltzmann–Gibbs entropy [22], and Barrow HDE models originate from Barrow's modification of the Bekenstein–Hawking entropy formula incorporating quantum gravitational corrections with a fractal horizon structure [23]. Recently, fractional holographic dark energy (FHDE) has been proposed [24], motivated by fractional entropy arising from fractional quantum mechanics in the context of Schwarzschild black hole thermodynamics [25], and it successfully describes the late time acceleration of the universe.

Beyond theoretical consistency, observational constraints are crucial for assessing the viability of HDE models, necessitating comparison with precise data, such as the Pantheon+ SN Ia sample [26–28] and observational Hubble parameter data (OHD) [29]. As standardizable candles, SN Ia allow for accurate distance measurements and were pivotal in revealing the late time acceleration of the universe. In parallel, OHD, inferred from galaxy ages or baryon acoustic oscillations, provide direct insights into the expansion history. As a result, researchers routinely combine SN Ia and OHD datasets as a powerful means of constraining cosmological parameters [30–51]. Recently, the Dark Energy Spectroscopic Instrument (DESI) collaboration released the baryon acoustic oscillation measure-

Received 24 June 2026; Accepted 12 August 2026; Accepted manuscript online 13 August 2026
* Supported by the National Natural Science Foundation of China (12405081, 11865018)
† E-mail: huangqihongzynu@163.com
©2026 Chinese Physical Society and the Institute of High Energy Physics of the Chinese Academy of Sciences and the Institute of Modern Physics of the Chinese Academy of Sciences and IOP Publishing Ltd. All rights, including for text and data mining, AI training, and similar technologies, are reserved.

ments from its second data release (DR2) [52], representing the largest spectroscopic galaxy sample to date. The DESI DR2 BAO measurements serve as a standard probe of the cosmic expansion history and are now widely used to constrain the dynamical properties of dark energy [53–74]. These high precision datasets serve to both test the consistency of dark energy models and to place stringent constraints on their key parameters. For the FHDE model, constraints from a combination of multiple observational datasets show that, with the model parameter $\alpha = 1$, it not only achieves late time accelerated expansion but also yields an age of the universe consistent with that of the standard ΛCDM model [75]. However, in the original FHDE formulation, the fractional parameter α is theoretically constrained to $1 < \alpha \leq 2$. It remains an open question whether this theoretically favored range is consistent with observational data. In addition, different choices of the IR cutoff can lead to qualitatively different cosmological evolutions [15]. In this paper, we systematically constrain three FHDE models with different IR cutoffs, namely the Hubble horizon, the future event horizon, and the particle horizon, using current observational datasets and assess their observational viability.

The goals of this paper are twofold: first, to constrain three FHDE models with different IR cutoffs using observational data and identify which models are observationally viable; second, to analyze the cosmological evolution of the viable model, including the evolution of the cosmological parameters and phase space dynamics, to understand its late time behavior and attractor structure. This paper is structured as follows. Section II introduces the FHDE models. Section III presents the observational constraints on the model parameters using the Pantheon+ SN Ia+OHD+DESI DR2+CMB dataset. Section IV investigates the cosmological evolution of these FHDE models, as well as its phase space dynamics and attractor behavior. Our main conclusions are summarized in Section V.

II. MODELS

Based on the holographic principle and the fractional entropy obtained from fractional quantum mechanics in the context of black hole thermodynamics [25], the FHDE energy density takes the form [24]

$$\rho_{\rm de} = 3C^2 L^{\frac{2-3\alpha}{\alpha}}, \tag{1}$$

where the fractional parameter α is constrained to $1 < \alpha \leq 2$ as derived from fractional quantum mechanics. This model reduces to the standard HDE for $\alpha = 2$, to Barrow HDE for $\alpha = \dfrac{2}{\Delta + 1}$, and to Tsallis HDE for $\alpha = \dfrac{2}{2\delta - 1}$.

We consider a homogeneous and isotropic Friedmann–Robertson–Walker universe, whose line element is given by

$$\mathrm{d}s^2 = -\mathrm{d}t^2 + a^2(t)(\mathrm{d}r^2 + r^2\mathrm{d}\Omega^2), \tag{2}$$

and the Friedmann equation takes the form

$$H^2 = \frac{\kappa^2}{3}\left(\rho_r + \rho_m + \rho_{\rm de}\right), \tag{3}$$

with ρ_r, ρ_m, and $\rho_{\rm de}$ denoting the energy densities of radiation, pressureless matter, and FHDE, respectively, and obeying the conservation equations

$$\dot{\rho}_r + 4H\rho_r = 0, \tag{4}$$

$$\dot{\rho}_m + 3H\rho_m = 0, \tag{5}$$

$$\dot{\rho}_{\rm de} + 3H(1 + \omega_{\rm de})\rho_{\rm de} = 0, \tag{6}$$

where the equation of state parameter $\omega_{\rm de}$ is defined as

$$\omega_{\rm de} = \frac{p_{\rm de}}{\rho_{\rm de}}. \tag{7}$$

After introducing the following dimensionless variables

$$\Omega_r = \frac{\kappa^2\rho_r}{3H^2}, \quad \Omega_m = \frac{\kappa^2\rho_m}{3H^2}, \quad \Omega_{\rm de} = \frac{\kappa^2\rho_{\rm de}}{3H^2}, \tag{8}$$

we can rewrite the Friedmann equation (3) as

$$\Omega_r + \Omega_m + \Omega_{\rm de} = 1. \tag{9}$$

Combining Eqs. (3)–(6) and (9) yields

$$\frac{\dot{H}}{H^2} = \frac{1}{2}\left[\Omega_m + (1 - 3\omega_{\rm de})\Omega_{\rm de}\right] - 2. \tag{10}$$

Combining Eqs. (5), (6), (9), and (10) with the definition $' = \dfrac{\mathrm{d}}{\mathrm{d}(\ln a)}$ yields the automatic dynamical equations governing this system

$$\Omega_m' = [(3\omega_{\rm de} - 1)\Omega_{\rm de} - \Omega_m + 1]\Omega_m, \tag{11}$$

$$\Omega_{\rm de}' = [(3\omega_{\rm de} - 1)(\Omega_{\rm de} - 1) - \Omega_m]\Omega_{\rm de}, \tag{12}$$

The deceleration parameter q is defined as

$$q = -1 - \frac{\dot{H}}{H^2}. \tag{13}$$

To constrain the model parameters using observational data and analyze the cosmological evolution based on the obtained constraints, we will analyze three FHDE models: (1) the original FHDE model with the Hubble horizon as the IR cutoff (FHDEH); (2) FHDE with the future event horizon as the IR cutoff (FHDEF); (3) FHDE with the particle horizon as the IR cutoff (FHDEP).

A. FHDEH

With the Hubble horizon chosen as the IR cutoff, the FHDEH energy density (1) becomes [24]

$$\rho_{\rm de} = 3C^2 H^{\frac{3\alpha-2}{\alpha}}. \tag{14}$$

Using Eqs. (6), (10), and (14), the equation of state parameter $\omega_{\rm de}$ can be solved as

$$\omega_{\rm de} = \frac{(3\alpha-2)(\Omega_m+\Omega_{\rm de})+8-6\alpha}{3[(3\alpha-2)\Omega_{\rm de}-2\alpha]}. \tag{15}$$

B. FHDEF

When the future event horizon is taken as the IR cutoff, the FHDEF energy density has the form

$$\rho_{\rm de} = 3C^2 R_F^{\frac{2-3\alpha}{\alpha}}, \tag{16}$$

with

$$R_F = a\int_t^{\infty}\frac{{\rm d}t}{a}, \tag{17}$$

which satisfies the relation $\dot{R}_F = HR_F - 1$. By combining Eqs. (6), (10), and (16), the equation of state parameter $\omega_{\rm de}$ can be derived as

$$\omega_{\rm de} = -\frac{1}{3\alpha}\Big[(3\alpha-2)F+2\Big], \tag{18}$$

with

$$F = \frac{1}{HR_F} = \frac{1}{C^{\frac{\alpha}{2-3\alpha}}}, \quad C = \frac{1}{\kappa^2 C^2}H^{\frac{2-\alpha}{\alpha}}\Omega_{\rm de} \tag{19}$$

which satisfies

$$F' = -\Big[\frac{1}{2}(\Omega_m+(1-3\omega_{\rm de})\Omega_{\rm de})-1-F\Big]F. \tag{20}$$

C. FHDEP

For the particle horizon as the IR cutoff, the FHDEP energy density takes the form

$$\rho_{\rm de} = 3C^2 R_P^{\frac{2-3\alpha}{\alpha}}, \tag{21}$$

with

$$R_P = a\int_0^t\frac{{\rm d}t}{a}, \tag{22}$$

which satisfies the relation $\dot{R}_P = HR_P + 1$. With Eqs. (6), (10), and (21), the equation of state parameter $\omega_{\rm de}$ can be expressed as

$$\omega_{\rm de} = \frac{1}{3\alpha}\Big[(3\alpha-2)P-2\Big], \tag{23}$$

with

$$P = \frac{1}{HR_P} = \frac{1}{C^{\frac{\alpha}{2-3\alpha}}}, \quad C = \frac{1}{\kappa^2 C^2}H^{\frac{2-\alpha}{\alpha}}\Omega_{\rm de}, \tag{24}$$

which satisfies

$$P' = -\Big[\frac{1}{2}(\Omega_m+(1-3\omega_{\rm de})\Omega_{\rm de})-1+P\Big]P. \tag{25}$$

III. OBSERVATIONAL CONSTRAINTS

In the previous section, we introduced three different FHDE models. In this section, we constrain the model parameters using four observational datasets: the Pantheon+ SN Ia sample covering the redshift range $z\in[0.001, 2.261]$[26–28], OHD sample spanning $z\in[0.07, 1.965]$ collected by [29] as shown in Table 1, BAO measurements from DESI DR2 covering $z\in[0.295, 2.33]$ [52], and CMB distance priors from Planck 2018 [76, 77].

A. Data and methodology

For these FHDE models, we can write the expansion rate function as

$$E(z) = \frac{H(z)}{H_0} = \sqrt{\Omega_{r,0}(1+z)^4+\Omega_{m,0}(1+z)^3+\Omega_{de,0}{\rm e}^{3\int_0^z\frac{1+\omega_{\rm de}}{1+z}{\rm d}z}}, \tag{26}$$

where $\Omega_{r,0}+\Omega_{m,0}+\Omega_{de,0}=1$. The theoretical apparent magnitude m_{th}, which corresponds to the predicted observable of SN Ia, is formulated as

$$m_{th} = 5\log_{10}\Big(\frac{D_L(z)}{Mpc}\Big)+25+M, \tag{27}$$

Table 1. OHD data [29].

z	$H(z)$/(km s^{-1} Mpc^{-1})	z	$H(z)$/(km s^{-1} Mpc^{-1})	z	$H(z)$/(km s^{-1} Mpc^{-1})	z	$H(z)$/(km s^{-1} Mpc^{-1})
0.07	69.0±19.6	0.28	88.8±36.6	0.4783	80.9±9.0	0.9	117.0±23.0
0.09	69.0±12.0	0.352	83.0±14.0	0.48	97.0±62.0	1.037	154.0±20.0
0.12	68.6±26.2	0.3802	83.0±13.5	0.593	104.0±13.0	1.3	168.0±17.0
0.17	83.0±8.0	0.4	95.0±17.0	0.68	92.0±8.0	1.363	160.0±33.6
0.179	75.0±4.0	0.4004	77.0±10.2	0.75	98.8±33.6	1.43	177.0±18.0
0.199	75.0±5.0	0.4247	87.1±11.2	0.781	105.0±12.0	1.53	140.0±14.0
0.2	72.9±29.6	0.4497	92.8±12.9	0.875	125.0±17.0	1.75	202.0±40.0
0.27	77.0±14.0	0.47	89.0±50.0	0.88	90.0±40.0	1.965	186.5±50.4

where M is the absolute magnitude of the SN Ia and $D_L(z)$ represents the luminosity distance, which is defined as

$$D_L(z) = c(1+z)\int_0^z \frac{\mathrm{d}z}{H(z)}. \tag{28}$$

To estimate the model parameters for these FHDE models, we perform Markov Chain Monte Carlo (MCMC) sampling with the emcee library in Python. For the FHDEH model, we constrain six parameters $\{H_0, \Omega_{m,0}, \Omega_{de,0}, \alpha, M, r_d\}$; for the FHDEF and FHDEP models, we constrain seven parameters $\{H_0, \Omega_{m,0}, \Omega_{de,0}, \alpha, C, M, r_d\}$. The total log-likelihood is defined as

$$\ln(\mathcal{L}_{\rm total}) = -\frac{1}{2}\chi^2_{\rm total} + const., \tag{29}$$

with

$$\chi^2_{\rm total} = \chi^2_{\rm SN} + \chi^2_{\rm OHD} + \chi^2_{\rm DESI} + \chi^2_{\rm CMB}. \tag{30}$$

Here, the χ^2 term for the SN Ia sample is given by

$$\chi^2_{\rm SN} = (\hat{m}_{\rm obs} - m_{\rm th})^{\dagger} C^{-1}_{\rm SN} (\hat{m}_{\rm obs} - m_{\rm th}), \tag{31}$$

where $\hat{m}_{\rm obs}$ denotes the array of observed corrected apparent magnitude, and $C_{\rm SN}$ represents the associated covariance matrix.

For the OHD sample, the χ^2 term is evaluated as

$$\chi^2_{\rm OHD} = \sum_{i=1}^{N_{\rm OHD}} \left(\frac{H_{{\rm obs},i} - H_{\rm th}(z_i)}{\sigma_{{\rm OHD},i}} \right)^2, \tag{32}$$

where $H_{{\rm obs},i}$ and $\sigma_{{\rm OHD},i}$ denote the i-th observed value and its standard deviation, respectively, and $N_{\rm OHD}$ is the total number of OHD data.

For the DESI DR2 sample, the χ^2 term is defined as

$$\chi^2_{\rm DESI} = \sum_{i=1}^{N_{\rm DESI}} \Delta_i^T \mathbf{C}_i^{-1} \Delta_i, \tag{33}$$

where the form of Δ_i and $\mathbf{C}_i$ depends on the measurement type provided for the i-th redshift bin. For anisotropic measurements, they are given by

$$\Delta_i = \begin{pmatrix} D_M^{\rm obs}(z_i)/r_d - D_M^{\rm th}(z_i)/r_d \\ D_H^{\rm obs}(z_i)/r_d - D_H^{\rm th}(z_i)/r_d \end{pmatrix} \tag{34}$$

and

$$\mathbf{C}_i = \begin{pmatrix} \sigma^2_{D_M/r_d} & r_{HM}\sigma_{D_M/r_d}\sigma_{D_H/r_d} \\ r_{HM}\sigma_{D_M/r_d}\sigma_{D_H/r_d} & \sigma^2_{D_H/r_d} \end{pmatrix}. \tag{35}$$

For isotropic measurements, Δ_i reduces to the scalar $D_V^{\rm obs}(z_i)/r_d - D_V^{\rm th}(z_i)/r_d$ with the corresponding variance $\sigma^2_{D_V/r_d}$. Here, the Hubble distance and the transverse comoving distance are defined as

$$D_H(z) = \frac{c}{H(z)}, \tag{36}$$

and

$$D_M(z) = c\int_0^z \frac{\mathrm{d}z}{H(z)}, \tag{37}$$

and the volume averaged distance $D_V(z)$ used in the isotropic case is given by

$$D_V(z) = \left[z D_M^2(z) D_H(z) \right]^{1/3}. \tag{38}$$

Here, σ_{D_M/r_d} and σ_{D_H/r_d} represent the observational uncertainties associated with $D_M(z)/r_d$ and $D_H(z)/r_d$, respectively, r_{HM} is their correlation coefficient between the two observables, and r_d is the sound horizon during the drag epoch.

For the CMB distance priors, the χ^2 term is given by

$$\chi^2_{\rm CMB} = \Delta p^T \mathbf{C}^{-1}_{\rm CMB} \Delta p, \qquad \Delta p = p^{\rm obs} - p^{\rm th}, \tag{39}$$

where $p=\{R,l_A,\Omega_b h^2\}$, with $\mathbf{C}_{\rm CMB}$ being the covariance matrix, and the CMB shift parameter R and the acoustic scale l_A take the form

$$R=\frac{D_M(z_*)\sqrt{\Omega_m H_0^2}}{c},\qquad l_A=\frac{\pi D_M(z_*)}{r_s(z_*)},\tag{40}$$

where z_* is the redshift at the photon decoupling epoch. According to Planck CMB observations, $p^{\rm obs}=\{1.7502, 301.471, 0.02236\}$. Since $\Omega_b h^2$ correlates with R and l_A, their covariance matrix, adopted from [77], is incorporated into the χ^2 calculation.

To compare the FHDE models with the standard ΛCDM model, we also perform a corresponding MCMC analysis of ΛCDM using the same observational datasets. Given the different numbers of parameters, we adopt the Akaike Information Criterion (AIC) [78] and Bayesian Information Criterion (BIC) [79, 80] to statistically compare these four models, where

$$\mathrm{AIC}=\chi^2_{\rm min}+2n,\tag{41}$$

and

$$\mathrm{BIC}=\chi^2_{\rm min}+n\ln(N),\tag{42}$$

where n is the number of parameters and N is the number of observational data points.

B. Results and discussion

To estimate the model parameters, we perform MCMC sampling using the emcee library in Python 3.13.14. The theoretical predictions are computed using our independently developed Python code. The burn-in is determined by the integrated autocorrelation time, discarding twice the maximum autocorrelation time, and convergence is ensured by requiring the chain length to exceed 50 times the autocorrelation time for all parameters. The prior ranges adopted for these parameters are $H_0\in[50,80]$, $\Omega_m\in[0.1,0.5]$, $\Omega_{\rm de}\in[0.5,0.9]$, $\alpha\in[1.0,2.0]$, $C\in[0.0,2.0]$, $M\in[-20,-18]$, and $r_d\in[130,160]$.

We summarize the parameter constraints for the ΛCDM, FHDEH, FHDEF, and FHDEP models in Table 2, where the mean values and 1σ confidence levels (CL) are listed. Three centered dots (⋯) in this table indicate that the mean values of α cannot be calculated because the observational constraints are nearly flat across the entire range $1<\alpha\leq 2$ derived from fractional quantum mechanics, indicating that all values in this interval are equally supported by the dataset. The posterior distributions for the FHDEH, FHDEF, and FHDEP models are presented in Figs. 1, 2, and 3, respectively. In these tables and figures, we adopt two datasets: SN+OHD+DESI DR2 and SN+OHD+DESI DR2+CMB. For the first dataset, the sound horizon at the drag epoch r_d is treated as a free parameter. For the second dataset, r_d is derived from the background model by the standard integration formula with the Planck 2018 best-fit value $z_{\rm drag}=1059.94$, and the sound horizon at the photon decoupling epoch r_* is computed using the standard integration formula with the Planck 2018 best-fit value $z_*=1089.92$ [8].

For the ΛCDM model, both datasets constrain the mean value of H_0 to 68.8km s^{-1} Mpc^{-1}, and the minimum $\chi^2_{\rm min}$ values are 1431.5 and 1437.3, respectively, indicating that the CMB distance priors are highly consistent with the low-redshift data within the ΛCDM framework, and adding the CMB distance priors does not shift the mean value.

When the dataset SN+OHD+DESI DR2 is used to constrain the FHDE models, for the FHDEH model, we obtain $H_0=67.9\pm1.7$km s^{-1} Mpc^{-1}, which is slightly lower than that in the ΛCDM model, and the parameter α is constrained to be $\alpha<1.164$; for the FHDEF model, we find H_0 has the same mean value as the FHDEH model,

Table 2. Summary of observational constraints (68% CL) for ΛCDM and FHDE models from different data combinations. The quantities $\Delta\chi^2_{\rm min}$, ΔAIC, and ΔBIC are defined with respect to ΛCDM, thus negative values favor the FHDE models, while positive values favor ΛCDM. The units of H_0 and r_d are km s^{-1} Mpc^{-1} and Mpc, respectively.

Datasets	Model	H_0	$\Omega_{m,0}$	$\Omega_{de,0}$	α	C	r_d	$\chi^2_{\rm min}$	$\Delta\chi^2_{\rm min}$	ΔAIC	ΔBIC
SN+OHD+DESI DR2	ΛCDM	$68.8^{+1.6}_{-1.7}$	$0.296^{+0.012}_{-0.009}$	$0.701^{+0.010}_{-0.009}$	–	–	147.1 ± 3.3	1431.5	0	0	0
	FHDEH	67.9 ± 1.7	$0.142^{+0.019}_{-0.035}$	$0.834^{+0.031}_{-0.022}$	<1.164	–	$147.0^{+3.4}_{-3.5}$	1426.7	−4.8	−2.8	2.6
	FHDEF	$67.9^{+1.5}_{-1.7}$	$0.205^{+0.055}_{-0.039}$	$0.775^{+0.029}_{-0.041}$	⋯	$0.525^{+0.145}_{-0.176}$	$147.0^{+3.4}_{-3.3}$	1426.8	−4.7	−0.7	10.1
	FHDEP	66.4 ± 1.6	$0.114^{+0.004}_{-0.014}$	$0.843^{+0.011}_{-0.005}$	<1.015	<0.029	$147.1^{+3.5}_{-3.4}$	1430.9	−0.6	3.4	14.2
SN+OHD+DESI DR2+CMB	ΛCDM	$68.8^{+1.5}_{-1.6}$	0.304 ± 0.004	$0.695^{+0.003}_{-0.004}$	–	–	–	1437.3	0	0	0
	FHDEH	62.1 ± 1.4	0.363 ± 0.004	0.637 ± 0.004	<1.002	–	–	1637.5	200.2	202.2	207.6
	FHDEF	$68.2^{+1.6}_{-1.7}$	0.309 ± 0.005	0.691 ± 0.005	<1.103	$1.062^{+0.077}_{-0.085}$	–	1436.5	−0.8	3.2	14
	FHDEP	$61.7^{+1.5}_{-1.4}$	$0.373^{+0.003}_{-0.004}$	0.627 ± 0.004	<1.002	<0.003	–	1687.8	250.5	254.5	265.3

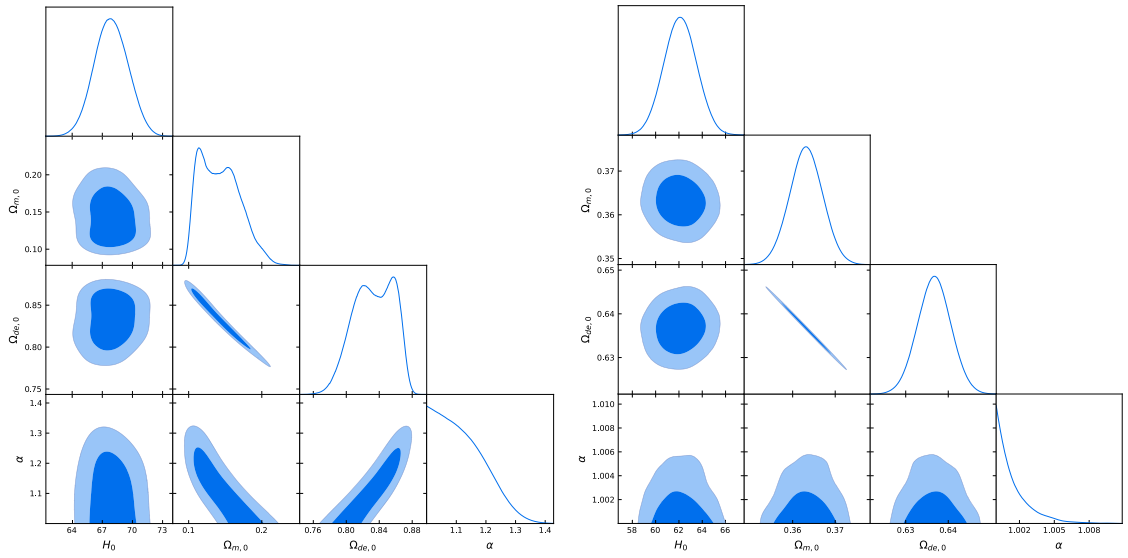


Fig. 1. (color online) Confidence contours for the parameters of the FHDEH model. The left panel uses SN, OHD, and DESI DR2 datasets, while the right panel uses SN, OHD, DESI DR2, and CMB distance priors. The units of H_0 are km s^{-1} Mpc^{-1}.

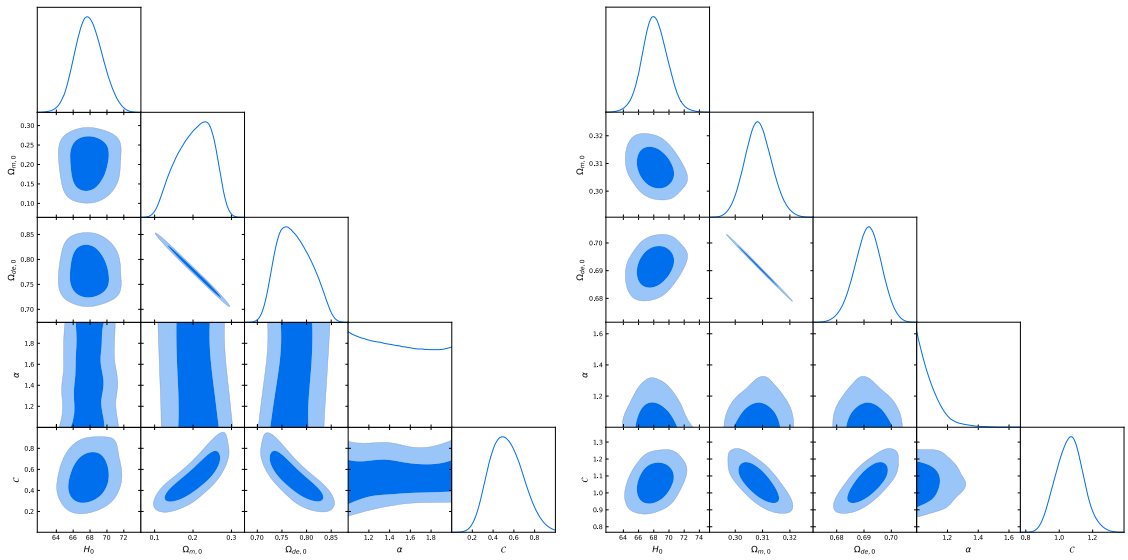


Fig. 2. (color online) Confidence contours for the parameters of the FHDEF model. The left panel uses SN, OHD, and DESI DR2 datasets, while the right panel uses SN, OHD, DESI DR2, and CMB distance priors. The units of H_0 are km s^{-1} Mpc^{-1}.

the parameter α is unconstrained, and the parameter C is constrained as $C = 0.525^{+0.146}_{-0.176}$; for the FHDEP model, it yields the lowest H_0 among all models, and yields stringent upper limits $\alpha < 1.015$ and $C < 0.029$. The minimum $\chi^2_{\rm min}$ values for FHDEH, FHDEF, and FHDEP are 1426.7, 1426.8, and 1430.9, respectively, all lower than that of the ΛCDM model, indicating that the FHDE models provide a marginally lower $\chi^2_{\rm min}$ than the ΛCDM model for this data combination. The ΔAIC values for FHDEH, FHDEF, and FHDEP are -2.8, -0.7, and 3.4, respectively, the AIC of FHDEH and FHDEF are slightly lower than that of the ΛCDM model, indicating a marginal preference according to the AIC criterion. The ΔBIC values for FHDEH, FHDEF, and FHDEP are 2.6, 10.1, and 14.2, respectively, all higher than that of the ΛCDM model, reflecting a penalty for the extra parameters α and C. These results indicate that the BIC strongly favors the ΛCDM model over the FHDEF and FHDEP models, and only slightly disfavors the FHDEH model.

When the dataset SN+OHD+DESI DR2+CMB, which includes the CMB distance priors, is used to constrain the FHDE models, for the FHDEH and FHDEP models, the parameter α is constrained to $\alpha < 1.002$ and the values of $\Delta\chi^2_{\rm min}$ exceed 200, indicating that both models are strongly disfavored by the data compared to the ΛCDM model at a very high significance level; for the

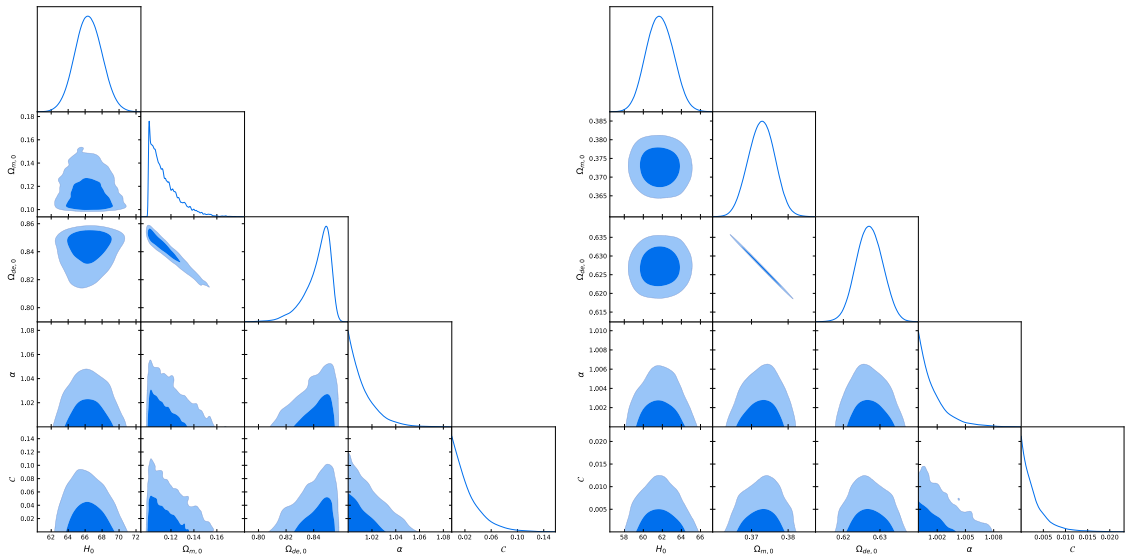


Fig. 3. (color online) Confidence contours for the parameters of the FHDEP model. The left panel uses SN, OHD, and DESI DR2 datasets, while the right panel uses SN, OHD, DESI DR2, and CMB distance priors. The units of H_0 are km s^{-1} Mpc^{-1}.

FHDEF model, we obtain $H_0 = 68.2^{+1.6}_{-1.7}$km s^{-1} Mpc^{-1}, which is slightly lower than that in the ΛCDM model, and the parameters α and C are constrained to be $\alpha < 1.103$ and $C = 1.062^{+0.077}_{-0.085}$. The values of $\Delta\chi^2_{\rm min}$, ΔAIC, and ΔBIC for FHDEF are −0.8, 3.2, and 14, respectively, suggesting that the FHDEF model provides a slightly lower $\chi^2_{\rm min}$ than the ΛCDM model, but the BIC strongly disfavors it compared to the ΛCDM model due to the penalty for extra parameters.

When comparing the constrained results from the datasets SN+OHD+DESI DR2 and SN+OHD+DESI DR2+CMB for the FHDEH and FHDEP models, we find when the CMB distance priors are introduced, H_0 is constrained to $H_0 = 62.1 \pm 1.4$ km s^{-1} Mpc^{-1} and $H_0 = 61.7^{+1.5}_{-1.4}$ km s^{-1} Mpc^{-1}, both of which are substantially smaller than that of the ΛCDM model, reflecting that this worsens the Hubble tension compared to the ΛCDM model; the parameter α is constrained to $\alpha < 1.002$ for both models, and the parameter C is constrained to $C < 0.003$ for the FHDEP model, both of which are very tight constraints; the values of $\Delta\chi^2_{\rm min}$ for the FHDEH and FHDEP models are 200.2 and 250.5, demonstrating that both models severely deviate from the ΛCDM model. As shown in Fig. 4, the comoving sound horizon $r_s(z)$ of the FHDEH and FHDEP models deviates significantly from the ΛCDM model, with the deviation becoming more pronounced toward lower redshifts. These results demonstrate that the FHDEH and FHDEP models show acceptable fits to low-redshift data (SN+OHD+DESI DR2) alone, but they catastrophically fail when CMB distance priors (high redshift) are added, as evidenced by $\Delta\chi^2_{\rm min} > 200$ and the clear discrepancy in r_s at $z \sim 1000$. This reveals that these models cannot reconcile the expansion history at recombination with that at late times, a capability that the ΛCDM model possesses. They are therefore strongly disfavored by the combined dataset, despite their low-redshift performance. However, in our previous work, when an interaction term is introduced to the FHDEH model, the resulting interacting FHDEH models yield a lower $\chi^2_{\rm min}$ than that of the ΛCDM model [81]. Therefore, introducing an interaction term between the pressureless matter and the dark energy is worth considering as a possible resolution for the FHDEH and FHDEP models.

We note that the poor performance of the FHDEH and FHDEP models is primarily driven by the CMB distance priors rather than the SN data, as shown in Table 2. Therefore, although we have used the Pantheon+ sample, we do not expect that the qualitative conclusions would

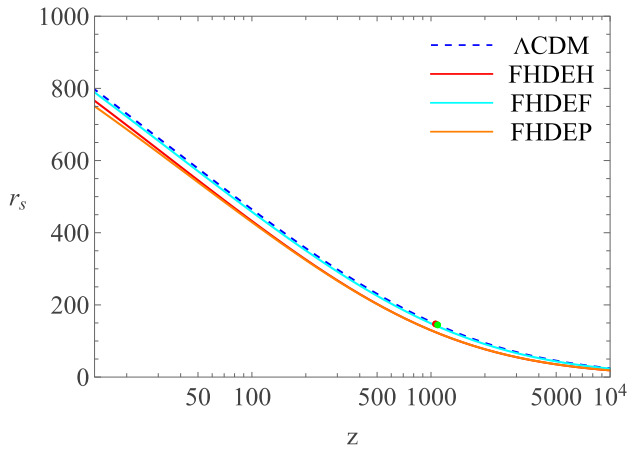


Fig. 4. (color online) Evolution of the comoving sound horizon r_s as a function of redshift z. The red and green dots represent the Planck 2018 values at baryon drag and recombination epochs, respectively. The unit of r_s is Mpc.

change with other SN Ia samples such as DESY5 or Union3, since the CMB constraints dominate.

In summary, using the SN+OHD+DESI DR2 dataset, FHDEH and FHDEF models provide fit statistics comparable to the ΛCDM model, with FHDEH exhibiting the best fit among the three FHDE models. However, when the number of free parameters is taken into account, the ΛCDM model remains statistically favored overall. When the CMB distance priors are included in the SN+OHD+DESI DR2+CMB dataset, the FHDEH and FHDEP models are strongly disfavored, while the FHDEF model remains the only FHDE model that survives the inclusion of CMB distance priors, although its ΔBIC indicates that it is still substantially penalized compared to the ΛCDM model.

IV. EVOLUTION OF THE UNIVERSE

In the previous section, we demonstrate that among the three FHDE models, only the FHDEF model survives the inclusion of CMB distance priors, while the FHDEH and FHDEP models are strongly ruled out by the observational data. In this section, we focus on the evolutionary behavior of the universe for these FHDE models using the mean values of the parameters obtained from the dataset SN+OHD+DESI DR2+CMB.

A. Evolution of cosmological parameters

To analyze the evolution of cosmological parameters, we adopt the mean values from Table 2 to solve the dynamical equation (11), (12), (20), and (25) for these FHDE models. We then plot the evolutionary curves of Ω_{de}, Ω_m, ω_{de}, and q for these FHDE models, as shown in Fig. 5, in which we show the evolutionary curve for the ΛCDM model with a blue dashed line and adopt the mean values for the ΛCDM model from Table 2.

In the first panel of Fig. 5, we can see that for all models, Ω_{de} approaches 0 at early times and tends to 1 at late times, indicating that FHDE models dominate the late time evolution of the universe. The second panel shows that Ω_m dominates at intermediate redshifts only for the FHDEF model; for the FHDEH and FHDEP models, Ω_m remains below 0.45 and does not play a dominant role; in all cases, Ω_m approaches 0 at late times. Overall, these two panels demonstrate that the FHDEF model exhibits only slight differences from the ΛCDM model in describing the evolution of Ω_{de} and Ω_m. In contrast, the FHDEH and FHDEP models fail to reproduce a pressureless matter dominated epoch. The third panel shows that ω_{de} for the FHDEH and FHDEP models behave as quintessence, but only the FHDEH model allows ω_{de} to approach -1 in the future; for the FHDEF model, ω_{de} behaves as quintessence in the past, has recently crossed the phantom divide, and currently lies in the phantom regime, indicating a quintom-like behavior that emerged at very late times. The fourth panel shows that the curves for the FHDEF and ΛCDM models overlap for $z > 0$, indicating that they share similar deceleration behavior in the past and at the present epoch; for the FHDEH model, the curve overlaps with the ΛCDM model for $z < 3$, but an obvious departure occurs for $z > 3$; for the FHDEP model, the curve departs from the ΛCDM model significantly; for all models, a transition from deceleration to acceleration can be realized in the expected redshift region ($0.48 \leq z_t < 1$). These results indicate that the FHDEF model is dynamically closest to ΛCDM among the three FHDE models, while the FHDEH and FHDEP models exhibit significant deviations that are consistent with their poor performance in the observational constraints.

For the FHDEF model, when $1+z$ approaches to 0, both ω_{de} and q decrease rapidly from -1.5 to more negative values, as shown in Fig. 5, indicating that the phantom behavior becomes increasingly severe in the future. Such an evolution inevitably leads to a divergence of the dark energy density ρ_{de} and the Hubble parameter $H(z)$ within a finite cosmic time, which is known as the big rip singularity. This behavior is qualitatively different from that of the ΛCDM model; its future evolution points toward a dramatic fate, offering a clear distinction from the standard cosmological paradigm.

In Fig. 6, adopting the mean values from the SN+OHD+DESI DR2+CMB dataset in Table 2, we plot the evolutionary curves of F for the FHDEF model and P for the FHDEP model. This figure shows that as $1+z$ approaches 0, corresponding to the infinite future, F increases, while P decreases to 0. This result means that, for the FHDEP model, P approaches 0 as $1+z$ approaches 0, indicating that the particle horizon diverges in the infinite future.

In summary, the FHDEF model predicts evolutions of Ω_{de} and Ω_m that are nearly identical to those of ΛCDM across the entire cosmic history. The deceleration parameter q also overlaps with that of ΛCDM for $z > 0$, indicating that the two models are cosmologically indistinguishable in the past and at the present epoch. However, ω_{de} for FHDEF has recently crossed the phantom divide and currently lies in the phantom regime, which will drive a future evolution of q that deviates from ΛCDM.

B. Attractor analysis

In the previous subsection, we have analyzed the evolution of cosmological parameters, and found that the FHDEF model closely mimics ΛCDM in the past and present, while the FHDEH and FHDEP models exhibit significant deviations; the equation of state parameter ω_{de} for the FHDEF model has recently crossed the phantom divide and entered the phantom regime, leading to a different future evolution. To further investigate this difference, we perform a dynamical system analysis of the attractor behavior for the FHDEF model.

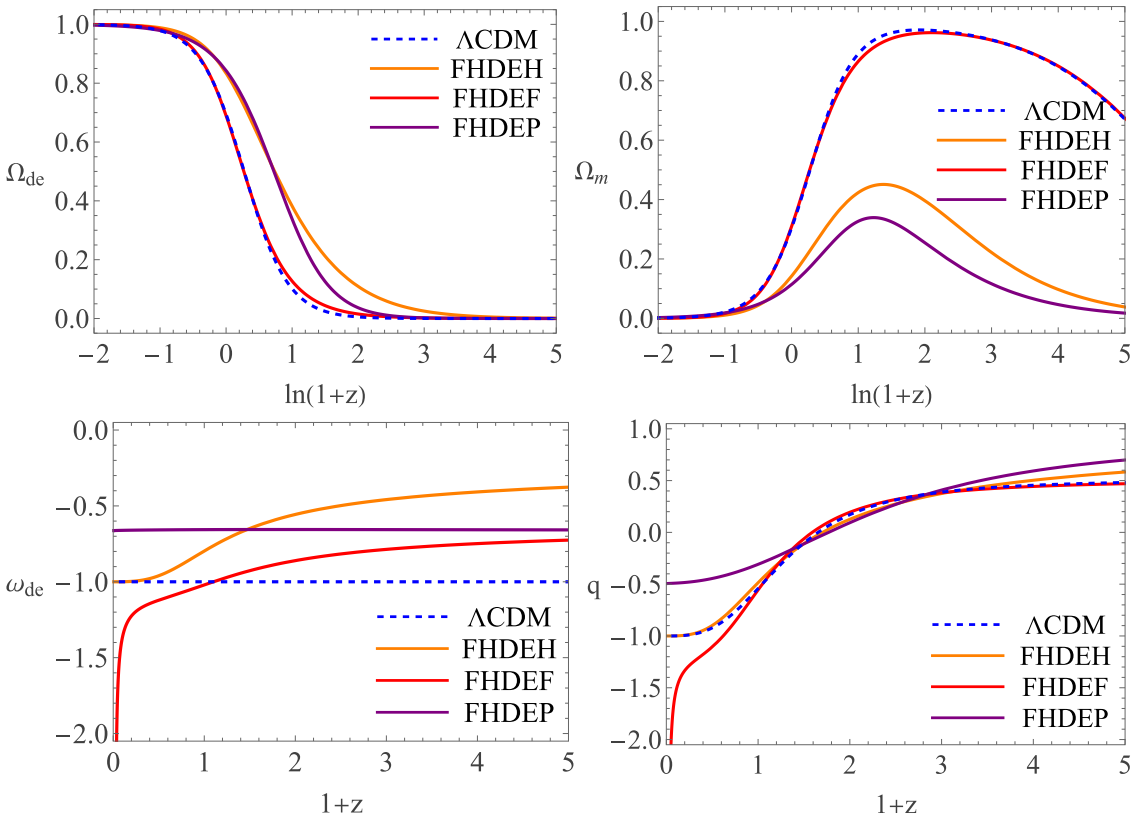


Fig. 5. (color online)Evolutionary curves of cosmological parameters for the FHDE models using the mean values from the SN+OHD+DESI DR2+CMB dataset.

To achieve this goal, following Refs. [82–90], we obtain the critical points by solving the autonomous system

$$\Omega'_m = \Omega'_{de} = F' = 0. \tag{43}$$

After solving Eqs. (11), (12), and (20), we obtain four critical points listed in Table 3. By linearizing the autonomous system, we derive a set of first order differential equations. The stability of the critical points is subsequently determined by the eigenvalues of the associated coefficient matrix. According to linear stability theory, a critical point is classified as an attractor if all eigenvalues are negative, as unstable if all are positive, and as a saddle point if the eigenvalues have mixed signs. Applying this criterion to the FHDEF model, we obtain the stability properties of the critical points which are summarized in Table 3.

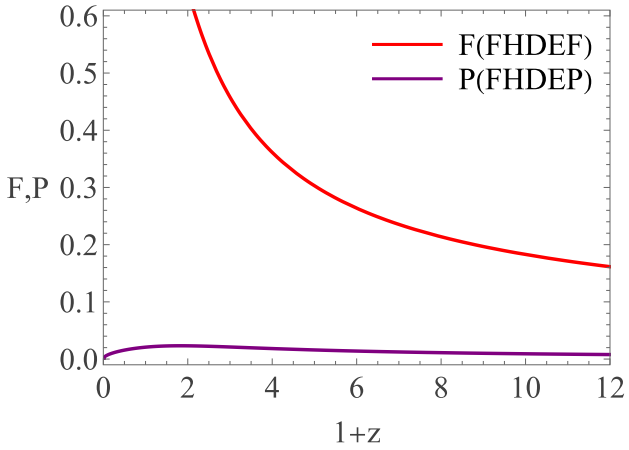


Fig. 6. (color online) Evolutionary curves of F for the FHDEF model and P for the FHDEP model using the mean values from the SN+OHD+DESI DR2+CMB dataset.

As shown by the summarized results in Table 3, point P_1 denotes a radiation dominated decelerated epoch, P_2 represents a pressureless matter dominated decelerated epoch, P_3 and P_4 correspond to the dark energy dominated acceleration epoch, as indicated by their corresponding values of q; among these, only the value of q for P_4 is equal to -1. For all points, the equation of state parameters ω_{de} are negative, and only the value of ω_{de} for P_4 reaches -1. Among these points, P_4 corresponds to the cosmological constant Λ, as it satisfies $q=-1$ and $\omega_{de}=-1$. The eigenvalue analysis further reveals that P_1 is an unstable node, P_2 and P_4 are saddle points, while P_3 is a stable attractor. This indicates that the FHDEF model admits a stable late time attractor P_3, consistent with the observed accelerated expansion, whereas the cosmological constant like point P_4 is only a saddle point and does

Table 3. Critical points and their stability for the FHDEF model.

Label	(Ω_m,Ω_{de},F)	Ω_r	ω_{de}	q	Eigenvalues	Conditions	Points
P_1	$(0,0,0)$	1	$-\frac{2}{3\alpha}$	1	$(1,1,\frac{2+\alpha}{\alpha})$	$1<\alpha\leq 2$	Unstable
P_2	$(1,0,0)$	0	$-\frac{2}{3\alpha}$	$\frac{1}{2}$	$(\frac{2}{\alpha},-1,\frac{1}{2})$	$1<\alpha\leq 2$	Saddle
P_3	$(0,1,0)$	0	$-\frac{2}{3\alpha}$	$\frac{1}{2}-\frac{1}{\alpha}$	$(-\frac{2}{\alpha},\frac{1}{2}-\frac{1}{\alpha},-\frac{2+\alpha}{\alpha})$	$1<\alpha<2$	Stable
P_4	$(0,1,1)$	0	-1	-1	$(-\frac{1}{2}+\frac{1}{\alpha},-4,-3)$	$1<\alpha<2$	Saddle

not serve as the final evolutionary state of the universe.

To analyze the evolution of the universe in the FHDEF model, we plot its phase space trajectories in the (Ω_m,Ω_{de}) plane using the mean parameter values from Table 2, as shown in Fig. 7. Figure 7 shows that the evolutionary trajectory for the FHDEF model overlaps with that of the ΛCDM model, and both evolve toward the same critical point $P_3/P_4(0,1)$. It should be noted that this point is a stable attractor for the ΛCDM model, while for the FHDEF model, P_3 is a stable point and P_4 is a saddle point.

To further investigate the evolution trajectories, we plot the phase space trajectories in the (Ω_m,Ω_{de},F) space for the FHDEF model in Fig. 8, with the mean parameter values from Table 2. In this figure, the green solid and red solid lines represent the ΛCDM and FHDEF models with the mean parameter values respectively, and the blue and purple solid lines correspond to the cases for the FHDEF model with $C=0.3$ and $C=0.8$, respectively. This figure shows that the value of C determines the behavior of the evolution trajectory on the F-axis. As C increases, the trajectory deviates further from the (Ω_m,Ω_{de}) plane. If C takes a value less than 0.8, the universe will eventually evolve into the stable attractor P_3, as shown by the blue and purple solid lines. According to the trajectory of the FHDEF model with the mean parameter values depicted by the red solid line, we can determine the evolution of the universe in the FHDEF model: the universe originates from the radiation dominated epoch P_1, then passes through the pressureless matter dominated epoch P_2 and the dark energy dominated epoch P_4 successively, and eventually evolves parallel to the F-axis with $\Omega_m=0$ and $\Omega_{de}=1$. Therefore, in the FHDEF model, after passing

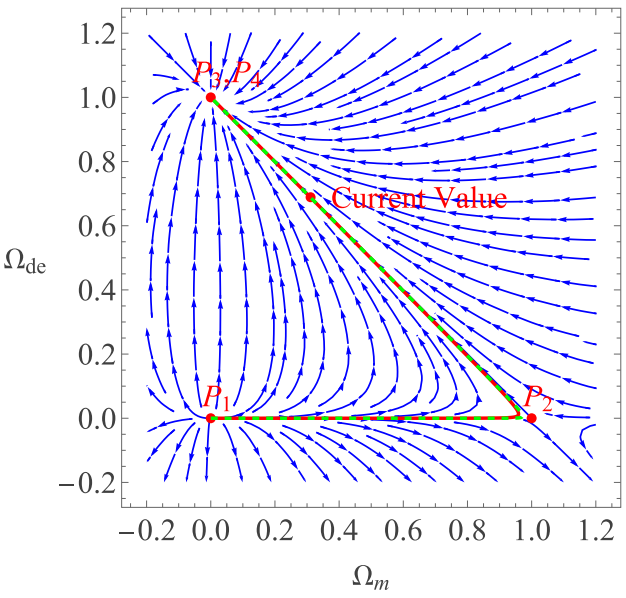


Fig. 7. (color online)Phase space trajectories in the (Ω_m,Ω_{de}) plane for the ΛCDM and FHDEF models, shown as green dashed and red solid lines respectively, with mean parameter values taken from Table 2.

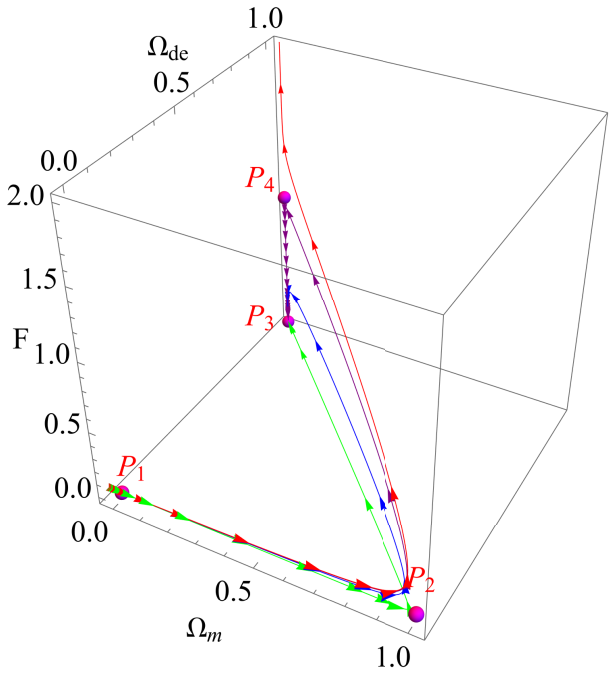


Fig. 8. (color online) Phase space trajectories in the (Ω_m,Ω_{de},F) space for the ΛCDM and FHDEF models, shown as green solid and red solid lines respectively, with mean parameter values taken from Table 2. The blue and purple solid lines correspond to the cases for the FHDEF model with $C=0.3$ and $C=0.8$, respectively.

through the ΛCDM-like evolutionary stages, the universe does not converge to P_3 but continues to evolve further, revealing a richer dynamical behavior beyond the standard ΛCDM cosmology.

V. CONCLUSIONS

Based on the fractional entropy derived from fractional quantum mechanics and taking the Hubble horizon as the IR cutoff, the FHDEH model has been proposed. When the model parameter α takes some special values, FHDEH can realize the late time acceleration of the universe. In this paper, we construct the FHDEF and FHDEP models by adopting the future event horizon and the particle horizon as the IR cutoff, respectively.

After using the SN, OHD, and DESI DR2 datasets to constrain the model parameters for the FHDEH, FHDEF, and FHDEP models, we obtain the mean values of these parameters, as well as $\chi^2_{\rm min}$, $\Delta\chi^2_{\rm min}$, ΔAIC, and ΔBIC for these models. Compared to the ΛCDM model, the minimum $\chi^2_{\rm min}$ values for these FHDE models are all lower than that of the ΛCDM model, indicating that the FHDE models provide a marginally lower $\chi^2_{\rm min}$ than ΛCDM for this data combination. Among the three FHDE models, FHDEH gives the smallest ΔAIC and ΔBIC values. The AIC values of FHDEH and FHDEF are slightly lower than that of the ΛCDM model, indicating a marginal preference according to the AIC criterion. The ΔBIC values for the FHDEH, FHDEF, and FHDEP models are 2.6, 10.1, and 14.2, respectively, all higher than that of the ΛCDM model, reflecting a penalty for the extra parameters α and C. These results indicate that the BIC strongly favors the ΛCDM model over the FHDEF and FHDEP models, and only slightly disfavors the FHDEH model.

When the dataset SN+OHD+DESI DR2+CMB, which includes the CMB distance priors, is used to constrain the FHDE models, the FHDEH and FHDEP models are strongly disfavored by the data, as the values of $\Delta\chi^2_{\rm min}$ exceed 200. For the FHDEF model, the values of $\Delta\chi^2_{\rm min}$, ΔAIC, and ΔBIC are -0.8, 3.2, and 14, respectively, suggesting that the FHDEF model yields a slightly lower $\chi^2_{\rm min}$ than ΛCDM model, but it is strongly disfavored by the BIC due to the penalty for extra parameters. However, our previous work suggests that introducing an interaction term to the FHDEH model can improve the fit to the data [81]. Therefore, extending the FHDEH and FHDEP models by including an interaction between pressureless matter and dark energy may provide a viable resolution to their incompatibility with CMB data.

Then, using the mean values obtained from the dataset SN+OHD+DESI DR2+CMB, we solve the corresponding dynamical equations and plot the evolutionary curves of cosmological parameters for the FHDE models. We find that the FHDEF model predicts evolutions of $\Omega_{\rm de}$ and Ω_m that are nearly identical to those of ΛCDM across the entire cosmic history, but q deviates from ΛCDM in the future, while the FHDEH and FHDEP models exhibit significant deviations.

To further investigate the evolution of the universe in the FHDEF model, we plot its phase space trajectories in the $(\Omega_m,\Omega_{\rm de})$ plane and the $(\Omega_m,\Omega_{\rm de},F)$ space using the mean parameter values from the dataset SN+OHD+DESI DR2+CMB. The evolution of the universe in the FHDEF model can be summarized as follows: the universe originates from the radiation dominated epoch P_1, then passes through the pressureless matter dominated epoch P_2 and the dark energy dominated epoch P_4 successively, and eventually evolves parallel to the F-axis with $\Omega_m = 0$ and $\Omega_{\rm de} = 1$. The results show that, after passing through the ΛCDM-like evolutionary stages, the universe does not converge to P_3 but continues to evolve further, revealing a richer dynamical behavior beyond the standard ΛCDM cosmology.

References

[1] S. Perlmutter, G. Aldering, G. Goldhaber *et al.*, Astrophys. J. **517**, 565 (1999)
[2] A. Riess, A. Filippenko, P. Challis *et al.*, Astron. J. **116**, 1009 (1998)
[3] D. Spergel, L. Verde, H. Peiris *et al.*, Astrophys. J. Suppl. **148**, 175 (2003)
[4] D. Spergel, R. Bean, O. Dore *et al.*, Astrophys. J. Suppl. **170**, 377 (2007)
[5] M. Tegmark, M. Strauss, M. Blanton *et al.*, Phys. Rev. D **69**, 103501 (2004)
[6] D. Eisenstein, I. Zehavi, D. Hogg *et al.*, Astron. J. **633**, 560 (2005)
[7] P. Peebles and B. Ratra, Rev. Mod. Phys. **75**, 559 (2003)
[8] N. Aghanim *et al.* (Planck Collaboration), A&A **641**, A6 (2020)
[9] S. Weinberg, Rev. Mod. Phys. **61**, 1 (1989)
[10] P. Steinhardt, L. Wang, and I. Zlatev, Phys. Rev. D **59**, 123504 (1999)
[11] A. Cohen, D. Kaplan, and A. Nelson, Phys. Rev. Lett. **82**, 4971 (1999)
[12] S. Hsu, Phys. Lett. B **594**, 13 (2004)
[13] M. Li, Phys. Lett. B **603**, 1 (2004)
[14] R. Horvat, Phys. Rev. D **70**, 087301 (2004)
[15] S. Wang, Y. Wang, and M. Li, Phys. Rep. **696**, 1 (2017)
[16] X. Zhang and F. Wu, Phys. Rev. D **72**, 043524 (2005)
[17] M. Li, X. Li, S. Wang, and X. Zhang, JCAP **06**, 036 (2009)
[18] T. Li, Y. Li, G. Du *et al.*, Eur. Phys. J. C **85**, 608 (2025)
[19] J. Li and S. Wang, JCAP **07**, 047 (2025)
[20] X. Zhang, Int. J. Mod. Phys. D **14**, 1597 (2005)
[21] Q. Huang and M. Li, JCAP **08**, 013 (2004)
[22] M. Tavayef, A. Sheykhi, K. Bamba *et al.*, Phys. Lett. B **781**, 195 (2018)
[23] E. Saridakis, Phys. Rev. D **102**, 123525 (2020)

[24] O. Trivedi, A. Bidlan, and P. Moniz, Phys. Lett. B **858**, 139074 (2024)
[25] S. Jalalzadeh, F. da Silva, and P. Moniz, Eur. Phys. J. C **81**, 1 (2021)
[26] A. Riess, W. Yuan, L. Macri *et al.*, Astrophys. J. Lett. **934**, L7 (2022)
[27] D. Brout, D. Scolnic, B.Popovic *et al.*, Astrophys. J. **938**, 110 (2022)
[28] D. Scolnic, D. Brout, A. Carr *et al.*, Astrophys. J. **938**, 113 (2022)
[29] S. Cao and B. Ratra, Mon. Not. R. Astron. Soc. **513**, 5686 (2022)
[30] X. Shen, B. Xu, K. Zhang *et al.*, Eur. Phys. J. C **85**, 992 (2025)
[31] J. Wang, H. Yu, and P. Wu, Eur. Phys. J. C **85**, 853 (2025)
[32] Y. Liu, H. Yu, and P. Wu, Phys. Rev. D **110**, L021304 (2024)
[33] Y. Liu, B. Wang, H. Yu *et al.*, Mon. Not. R. Astron. Soc. **533**, 244 (2024)
[34] S. Arora and P. Sahoo, Phys. Dark Universe **45**, 101510 (2024)
[35] A. Oliveros and M. Acero, Int. J. Mod. Phys. D **33**, 2450004 (2024)
[36] D. Wang, M. Koussour, A. Malik *et al.*, Eur. Phys. J. C **83**, 670 (2023)
[37] P. Mukherjee and N. Banerjee, Phys. Dark Universe **36**, 100998 (2022)
[38] P. Mukherjee and N. Banerjee, Phys. Rev. D **105**, 063516 (2022)
[39] S. Cao, J. Ryan, and B. Ratra, Mon. Not. R. Astron. Soc. **504**, 300 (2021)
[40] S. Pacif, S. Arora, and P. Sahoo, Phys. Dark Universe **32**, 100804 (2021)
[41] S. Cao, T. Zhang, X. Wang *et al.*, Universe **7**, 57 (2021)
[42] O. Akarsu, J. Barrow, L. Escamilla *et al.*, Phys. Rev. D **101**, 063528 (2020)
[43] Y. Yang and Y. Gong, JCAP **06**, 59 (2020)
[44] Y. Liu, R. Guo, J. Zhang *et al.*, JCAP **05**, 016 (2019)
[45] J. Jimenez, R. Lazkoz, D.Saez-Gomez *et al.*, Eur. Phys. J. C **76**, 631 (2016)
[46] Y. Gong, Q. Gao, and Z. Zhu, Mon. Not. R. Astron. Soc. **430**, 3142 (2013)
[47] Q. Su, Z. Tuo, and R. Cai, Phys. Rev. D **84**, 103519 (2011)
[48] Y. Gong, R. Cai, Y. Chen, and Z. Zhu, JCAP **01**, 019 (2010)
[49] P. Wu and H. Yu, Phys. Lett. B **693**, 415 (2010)
[50] Y. Gong and A. Wang, Phys. Rev. D **73**, 083506 (2006)
[51] P. Wu and H. Yu, Phys. Lett. B **643**, 315 (2006)
[52] M. Abdul Karim, J. Aguilar, S. Ahlen *et al.*, Phys. Rev. D **112**, 083515 (2025)
[53] T. Li, G. Du, Y. Li *et al.*, Sci. China Phys. Mech. Astron. **69**, 210413 (2026)
[54] T. Li, G. Du, S. Zhou *et al.*, Phys. Dark Universe **52**, 102254 (2026)
[55] T. Li, W. Giare, G. Du *et al.*, arXiv: 2601.07361
[56] T. Li, G. Du, H. Wang *et al.*, Res. Astron. Astrophys. **26**, 084002 (2026)
[57] G. Du, T. Li, T. Liu *et al.*, Sci. China Phys. Mech. Astron. **69**, 280411 (2026)
[58] X. Ren, S. Li, Y. Liu *et al.*, Res. Astron. Astrophys. **26**, 084001 (2026)
[59] H. Wang and Y. Piao, Phys. Lett. B **873**, 140180 (2026)
[60] J. Wang, R. Cai, Z. Guo *et al.*, Phys. Rev. D **113**, 083534 (2026)
[61] G. Du, T. Li, P. Wu *et al.*, arXiv: 2507.16589
[62] T. Li, P. Wu, G. Du *et al.*, ApJ **976**, 1 (2024)
[63] Y. Pang, X. Zhang, and Q. Huang, Sci. China Phys. Mech. Astron. **68**, 280410 (2025)
[64] H. Wang and Y. Piao, arXiv: 2511.16606
[65] M. Yadav, A. Dixit, M. Barak *et al.*, JHEAp **50**, 100514 (2026)
[66] Z. Zhu, Q. Jiang, Y. Liu *et al.*, JHEAp **51**, 100377 (2026)
[67] F. Plaza, G. Leon, and L. Kraiselburd, Eur. Phys. J. C **85**, 1262 (2025)
[68] V. Petri, V. Marra, and R. Marttens, Phys. Rev. D **113**, 023504 (2026)
[69] T. Li, P. Wu, G. Du *et al.*, Phys. Dark Universe **50**, 102068 (2025)
[70] J. Li and S. Wang, Eur. Phys. J. C **85**, 1308 (2025)
[71] Y. Li and X. Zhang, JCAP **12**, 018 (2025)
[72] T. Li, Y. Zhang, Y. Yao *et al.*, JCAP **12**, 048 (2025)
[73] G. Luciano, A. Paliathanasis, and E. Saridakis, JHEAp **49**, 100427 (2026)
[74] Y. Wang and K. Freese, JCAP **02**, 023 (2026)
[75] R. Robles-Barba, A. Garcia-Rivera, L. Molina-Ponce *et al.*, Phys. Scr. **100**, 085030 (2026)
[76] Z. Zhai and Y. Wang, JCAP **07**, 005 (2019)
[77] L. Chen, Q. Huang, and K. Wang, JCAP **02**, 028 (2019)
[78] H. Akaike, IEEE Trans. Automatic Control **19**, 716 (1974)
[79] G. Schwarz, Ann. Stat. **6**, 461 (1978)
[80] R. Trotta, Contemp. Phys. **49**, 71 (2008)
[81] Q. Huang, H. Chen, and Q. Wu, Universe **12**, 134 (2026)
[82] S. Bahamonde, C. Bohmer, S. Carloni *et al.*, Phys. Rep. **1**, 775 (2018)
[83] Q. Huang, H. Huang, J. Chen *et al.*, Class. Quantum Grav. **36**, 175001 (2019)
[84] Q. Huang, H. Huang, B. Xu *et al.*, Eur. Phys. J. C **81**, 686 (2021)
[85] P. Wu and H. Yu, Phys. Lett. B **692**, 176 (2010)
[86] J. Dutta, W. Khyllep, and N. Tamanini, Phys. Rev. D **95**, 023515 (2017)
[87] P. Wu and S. Zhang, JCAP **06**, 007 (2008)
[88] P. Wu, and H. Yu, Class. Quant. Grav. **24**, 4661 (2007)
[89] Q. Huang, H. Huang, B. Xu *et al.*, Universe **11**, 147 (2025)
[90] Q. Huang, H. Huang, B. Xu *et al.*, Eur. Phys. J. C **85**, 395 (2025)